Extra long imaging range swept source optical coherence tomography using re-circulation loops

Adrian Bradu,* Liviu Neagu and Adrian Podoleanu

Applied Optics Group, School of Physical Sciences, University of Kent, Canterbury, Kent, CT2 7NH, UK
*a.bradu@kent.ac.uk

Abstract: One of the main drawbacks of the swept source optical coherence tomography (SS-OCT) is its limited axial range. A novel interferometer configuration is proposed, equipped in each arm with an adjustable path length ring. By compensating the losses in the rings using semiconductor optical amplifiers, multiple paths A-scans can be obtained which when combined axially, can lead to an extremely long overall axial range. The effect of the re-circulation loops is equivalent with extending the coherence length of the swept source. In this way, the axial imaging range in SS-OCT can be pushed well beyond the limit imposed by the coherence length of the laser, to exceed in principle many centimeters.

OCIS codes: (110.4500) Optical coherence tomography; (250.5980) Semiconductor optical amplifiers.

References and links

1. R. A. Leitgeb, C. K. Hitzenberger, and A. Fercher, "Performance of fourier domain vs. time domain optical coherence tomography," Opt. Express **11**(8), 889–894 (2003), http://www.opticsinfobase.org/oe/abstract.cfm?URI=oe-11-18-2190.
2. J. F. de Boer, B. Cense, B. H. Park, M. C. Pierce, G. J. Tearney, and B. E. Bouma, "Improved signal-to-noise ratio in spectral-domain compared with time-domain optical coherence tomography," Opt. Lett. **28**(21), 2067–2069 (2003).
3. M. A. Choma, M. V. Sarunic, C. Yang, and J. A. Izatt, "Sensitivity advantage of swept source and Fourier domain optical coherence tomography," Opt. Express **11**(18), 2183–2189 (2003), http://www.opticsinfobase.org/oe/abstract.cfm?URI=oe-11-18-2183.
4. S. H. Yun, G. J. Tearney, B. E. Bouma, B. H. Park, and J. de Boer, "High-speed spectral-domain optical coherence tomography at 1.3 mum wavelength," Opt. Express **11**(26), 3598–3604 (2003), http://www.opticsinfobase.org/oe/abstract.cfm?URI=oe-11-26-3598.
5. S. H. Yun, G. J. Tearney, J. F. de Boer, N. Iftimia, and B. E. Bouma, "High-speed optical frequency-domain imaging," Opt. Express **11**(22), 2953–2963 (2003), http://www.opticsinfobase.org/oe/abstract.cfm?URI=oe-11-22-2953.
6. K. Aljasem, A. Werber, A. Seifert, and H. Zappe, "Fiber optic tunable probe for endoscopic optical coherence tomography," J. Opt. A, Pure Appl. Opt. **10**(4), 044012 (2008).
7. J. J. Armstrong, M. S. Leigh, D. D. Sampson, J. H. Walsh, D. R. Hillman, and P. R. Eastwood, "Quantitative upper airway imaging with anatomic optical coherence tomography," Am. J. Respir. Crit. Care Med. **173**(2), 226–233 (2005).
8. J. A. Goldsmith, Y. Li, M. R. Chalita, V. Westphal, C. A. Patil, A. M. Rollins, J. A. Izatt, and D. Huang, "Anterior chamber width measurement by high-speed optical coherence tomography," Ophthalmology **112**(2), 238–244 (2005).
9. M. Wojtkowski, A. Kowalczyk, R. Leitgeb, and A. F. Fercher, "Full range complex spectral optical coherence tomography technique in eye imaging," Opt. Lett. **27**(16), 1415–1417 (2002).
10. J. Zhang, W. Jung, J. S. Nelson, and Z. Chen, "Full range polarization-sensitive Fourier domain optical coherence tomography," Opt. Express **12**(24), 6033–6039 (2004), http://www.opticsinfobase.org/abstract.cfm?URI=oe-12-24-6033.
11. E. Götzinger, M. Pircher, R. Leitgeb, and C. Hitzenberger, "High speed full range complex spectral domain optical coherence tomography," Opt. Express **13**(2), 583–594 (2005), http://www.opticsinfobase.org/oe/abstract.cfm?URI=oe-13-2-583.
12. A. M. Davis, M. A. Choma, and J. A. Izatt, "Heterodyne swept-source optical coherence tomography for complete complex conjugate ambiguity removal," J. Biomed. Opt. **10**(6), 064005 (2005).

#135647 - $15.00 USD Received 24 Sep 2010; revised 4 Nov 2010; accepted 12 Nov 2010; published 19 Nov 2010

13. A. Bachmann, R. Leitgeb, and T. Lasser, "Heterodyne Fourier domain optical coherence tomography for full range probing with high axial resolution," Opt. Express **14**(4), 1487–1496 (2006), http://www.opticsinfobase.org/oe/abstract.cfm?URI=oe-14-4-1487.
14. B. Hofer, B. Považay, B. Hermann, A. Unterhuber, G. Matz, and W. Drexler, "Dispersion encoded full range frequency domain optical coherence tomography," Opt. Express **17**(1), 7–24 (2009), http://www.opticsinfobase.org/oe/abstract.cfm?URI=oe-17-1-7.
15. B. Hofer, B. Považay, A. Unterhuber, L. Wang, B. Hermann, S. Rey, G. Matz, and W. Drexler, "Fast dispersion encoded full range optical coherence tomography for retinal imaging at 800 nm and 1060 nm," Opt. Express **18**(5), 4898–4919 (2010), http://www.opticsinfobase.org/oe/abstract.cfm?URI=oe-18-5-4898.
16. D. Woods, and A. Podoleanu, "Controlling the shape of Talbot bands' visibility," Opt. Express **16**(13), 9654–9670 (2008), http://www.opticsinfobase.org/oe/abstract.cfm?URI=oe-16-13-9654.
17. S. Makita, T. Fabritius, and Y. Yasuno, "Full-range, high-speed, high-resolution 1 microm spectral-domain optical coherence tomography using BM-scan for volumetric imaging of the human posterior eye," Opt. Express **16**(12), 8406–8420 (2008), http://www.opticsinfobase.org/oe/abstract.cfm?URI=oe-16-12-8406.
18. L. Neagu, A. Bradu, L. Ma, J. W. Bloor, and A. G. Podoleanu, "Multiple-depth en face optical coherence tomography using active recirculation loops," Opt. Lett. **35**(13), 2296–2298 (2010).

1. Introduction

One of the main drawbacks of the spectral domain optical coherence tomography (SD-OCT) [1–3] is its limited imaging range. In Fourier domain (FD)-OCT this limitation is due to the finite spectral resolution of the spectrometer and (or) the pixel width of the line-scan camera [4]. In swept source (SS)-OCT imaging systems, the spectral resolution is determined by the instantaneous line-width of the swept source [5]. Narrow line-width SSs have been reported, which makes SS-OCT more suitable to imaging long axial samples than FD-OCT. Long axial range imaging is necessary in endoscopy, small animal imaging, or anterior segment imaging of the human eye where at least 1 cm axial range with good sensitivity is required [6–8].

In SS-OCT, by pushing the tuning speed high, the coherence length associated with the instantaneous line-width suffers. The finite coherence length causes the visibility of the interference fringe to decrease as the optical path difference (OPD) in between the reference arm length and object arm length of the interferometer increases. This leads to a decay of signal-to-noise ratio with OPD that limits the useful ranging depth. Moreover, the incapacity to distinguish in between positive and negative electrical frequencies leads to ambiguity between negative and positive depths (mirror terms).

A solution to eliminate the mirror terms and consequently to improve the axial imaging range in both SS-OCT and FD-OCT, lies in constructing the complex spectrum of the photo-detected signal. In this way, the axial range is doubled and the images can be positioned around zero-OPD [9]. Several techniques have been demonstrated capable to eliminate these artifacts and obtain full range images by using phase modulators [10,11], frequency shifters [12,13], numerical methods [14,15], using Talbot bands effect [16] or the BM-scan technique [17], etc.

The limitation of the techniques listed above is the fact that they only lead to a potential twofold increase in the axial range.

Here, we propose a novel configuration that allows (a) simultaneous interogation of multiple depths separated by an interval adjustable from zero to values less, larger or much larger than the coherence length of the swept source and (b) increase of the axial imaging range beyond the limit imposed by the coherence length of the SS. By using re-circulation loops in both sample and reference arms of the interferometer, theoretically an infinetly long imaging range can be achieved. A time domain OCT configuration with multiple re-circulations was previously reported [18] which under broadband excitation can be used to generate simultaneously multiple en-face OCT images from different depths in the sample. A slightly modified configuration is employed in this paper, where we demonstrate that novel and total different functionality is achieved when using a swept source.

#135647 - $15.00 USD Received 24 Sep 2010; revised 4 Nov 2010; accepted 12 Nov 2010; published 19 Nov 2010

2. Method

Light from a swept source, central wavelength 1060 nm, maximum sweeping range 60 nm, instanteneous line-width 0.05 nm, which determines an associated coherence lengths of around 20 mm (Broadsweeper 1060, Superlum, Cork, Ireland) is split into a main sample arm and a main reference arm by the directional coupler DC, which feeds a Mach-Zehnder interferometer set-up. In each arm of the interferometer, a separate optical ring, with an adjustable path length is placed. Each ring incorporates an acousto-optic frequency shifter (AOFS1 and AOFS2) that shifts the optical frequency upward by the frequency of the driving signal f1 (f2). To compensate for losses, semiconductor optical amplifiers (SOA1 and SOA2, QPhotonics, QSOA-1050) are incorporated in the two rings. In this way, multiple depths can simultaneously be interrogated, separated by the difference between the optical path lengths of the two rings, OPD_R. In comparison to the configuration reported in [18], attenuation in the rings was reduced by moving the AOFS away from the main loop. This has allowed utilisation of a single coupler instead of two in each ring. Additionally, this also allows comparison of the novel functionality (determined by the rings) with that achievable using a standard SS-OCT configuration (based on the interference between the waves in the main loop).

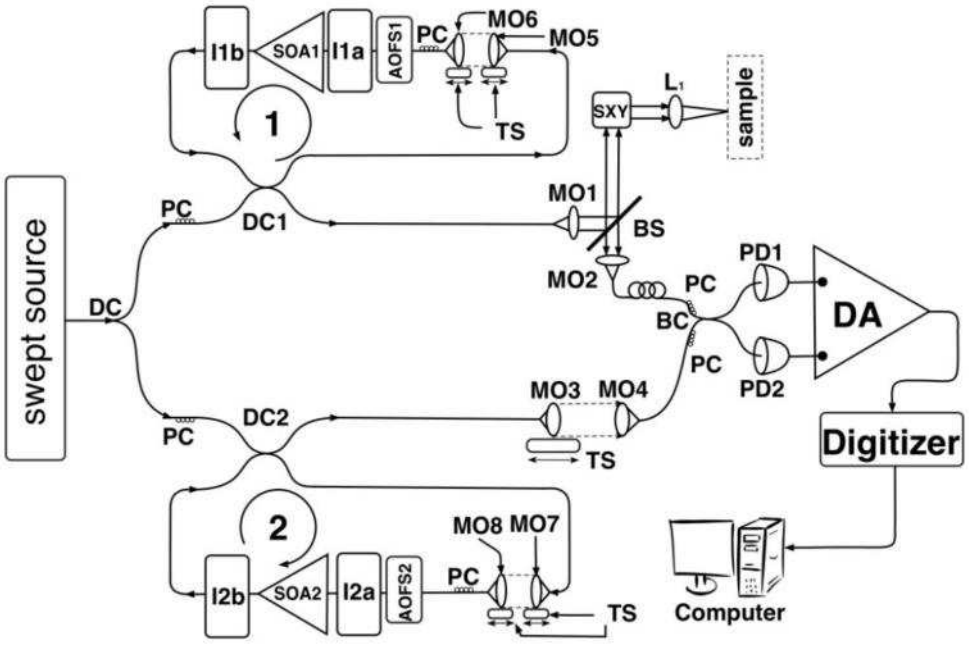

Fig. 1. Anatomy of the multiple-depth SS-OCT system: DC, DC1,2, BC: 50:50 directional couplers, PC: polarization controllers, I1,2(a,b): optical isolators, SOA1,2: semiconductor optical amplifiers, AOFS1,2: acusto-optic frequency shifters, MO1-8: microscope objectives, TS: translation stages, L1: achromatic lens, BS: beam-splitter, PD1,2: photo-detectors, DA: differential amplifier, SXY: galvo-scanner.

The optical path lengths in the rings and their difference OPD_R can be adjusted by actuating on the micrometer screws of the translation stages TS incorporated in the rings, which allow axial movement of the launchers holding the microscope objectives (MO5-MO8) and respective optical fiber apertures.

Optical isolators I1a,b (I2a,b) placed at the input and at the output of the SOA1 (SOA2) protect their operation from stray reflection. The injection of light into the rings and the reinjection of the amplified light into the main loop take place in the directional coupler DC1 (DC2). For every pass of the light through the two rings, the optical frequency is shifted by f1

#135647 - $15.00 USD Received 24 Sep 2010; revised 4 Nov 2010; accepted 12 Nov 2010; published 19 Nov 2010

(f2). The main sample arm contains a beam-splitter (BS), two microscope objectives (MO1 and MO2), a galvo-scanner (SXY) and an achromatic lens (L1, focal length 3.5 cm) to convey light to and back from the object. The optical power on the sample from the swept source was 400 µW. With the SOA1 on, the optical power on the sample increased to 550 µW. The multiple waves from the reference path interfere with the multiple waves from the sample path at the directional coupler BC, producing a beat at $|f1-f2| = n \cdot \Delta f$, where n is the number of re-circulations of light in the two rings. The BC output signals are sent to a balanced photo-detector unit, consisting of two photo-detectors (PD1 and PD2), and a differential amplifier (DA) which allows for removal of non-interferometric signals.

The output of DA was digitized using a 12-bit analog-to-digital acquisition card (National Instruments, Austin, Texas, PCI-5124). The digitizer was triggered for each A-scan, synchronously with the TTL signal associated with the signal which drives the tunable filter of the swept source.

Multiple signals placed around carriers of frequency $n \cdot \Delta f$ are all present in the photo-detected signal. The Fast Fourier Transform (FFT) of the signal leads to the A-scan corresponding to the interference of signals from the main loop (the non re-circulated light) as well as to the A-scans corresponding to the re-circulations.

3. Results and discussions

Figure 2 depicts the FFT of the photo-detected signal when a flat mirror is used as object, for an OPD = 0 in the main loop and $OPD_R = 0$ in the rings. The two AOFS were driven initially at f1 = 40 MHz and f2 = 40.5 MHz. The component around 0 Hz (order n = 0) corresponds to the interference of waves originating from the main loop only (not re-circulated) while the other peaks at multiples of Δf = 500 kHz (orders n = 1, 2, 3, 4 and 5) are generated by interference of similar orders, n, of re-circulation waves in the rings. Depending on the balance of gain and losses in the rings, only a limited number of round trips can be achieved, as shown in our previous report on a similar configuration excited by a broadband source [18]. An attenuation of 6 - 8 dB is noticed from one recirculation to the next.

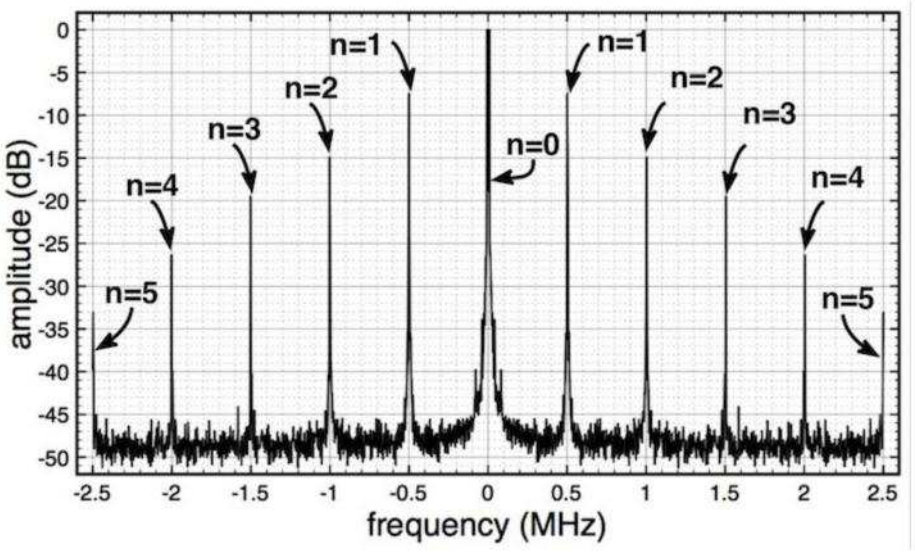

Fig. 2. FFT of the photo-detected signal for $OPD_R = OPD = 0$. Each component represents the carrier $n \cdot \Delta f$ of an independent OCT channel.

By increasing the OPD in the main loop, all frequency components in Fig. 2 move to the right by the same frequency, F:

#135647 - $15.00 USD Received 24 Sep 2010; revised 4 Nov 2010; accepted 12 Nov 2010; published 19 Nov 2010

$$F = C \cdot OPD, \tag{1}$$

as determined by a factor C, where C is the conversion factor from OPD to radio-frequency due to scanning the number of peaks in the channeled spectrum determined by the given OPD. The frequency generated F is:

$$F = \frac{\Delta k}{2\pi} \cdot \gamma \cdot OPD = C \cdot OPD, \tag{2}$$

where Δk is the tuning bandwidth in wave-number and γ is the scanning rate in Hz. The coefficient C is determined by the swept source, i.e. by its scanning speed and tuning bandwidth. The larger the tuning bandwidth, Δk and the scanning speed, γ, the larger the frequency F generated, i.e. the number of cycles in the photo-detected signal for a given OPD value. For settings on the source: λ_{min} = 1030 nm, λ_{max} = 1080 nm and a sweeping speed = 10,000 nm/s, this gives γ = 200 Hz. Theoretically, for these values C = 8.989 kHz/mm. Experimentally we determined C by increasing the OPD until the frequencies moved by 100 kHz and obtained an OPD = 11.05 mm. This gives an experimental value for C = 9.05 kHz/mm.

If the OPD is made negative, then all components apart from the fundamental move to the left. This property can allow elimination of mirror terms [12,13]. As there is no AOFS in the main loop, the interference of the two beams in the main loop exhibits mirror terms, and therefore, irrespective of the OPD sign, the peak of initial frequency zero will move to the right. However, on all secondary peaks, detection free of mirror terms can take place.

By increasing the OPD_R, the peak for n = 0 does not move, while the frequency peaks in Fig. 2 corresponding to the interfering re-circulating waves will move in OPD by $n \cdot OPD_R$ and in frequency by $n \cdot C \cdot OPD_R$.

The frequencies F_n of each channel n (corresponding to interference of n round trips in the rings and for n = 0 in the main loop) are given by:

$$F_n = n \cdot \Delta f + C \cdot (OPD + n \cdot OPD_R). \tag{3}$$

In Fig. 2, for OPD = OPD_R = 0, all channels exhibit frequencies $F_n = n \cdot \Delta f = n \cdot 500$ kHz.

The next set of measurements was collected for OPD_R = - 10 mm (i.e. by making the path length of the object ring in the re-circulating object arm longer by 10 mm than the length of the reference ring, in the re-circulating reference arm) in which case interference for the re-circulating waves traversing the secondary loops once will exhibit a maximum at OPD = 10 mm (given by OPD + OPD_R = 0) the re-circulating waves traversing the secondary loops twice will exhibit an interference maximum at OPD = 20 mm (given by OPD + $2 \cdot OPD_R$ = 0), and so on.

For any given OPD and OPD_R, the deviation of each channel frequency from its own carrier frequency is:

$$\Delta F_n = C \cdot (OPD + n \cdot OPD_R). \tag{4}$$

Next, we adjusted the carrier frequency to Δf = 250 kHz and maintained OPD_R = - 10 mm. Figure 3a illustrates the profiles of sensitivity of A-scans demodulated around four carrier frequencies $n \cdot \Delta f$ with n = 0, 1, 2. For OPD + $n \cdot OPD_R$ = 0, the frequencies of the signals in each channel are $n\Delta f$ according to (3). At the maximum, order n = 1 has Δf = 250 kHz in OPD = 10 mm and order n = 2 reaches maximum for OPD = 20 mm, where it exhibits $2 \cdot \Delta f$ = 500 kHz and so on. The maxima correspond to global optical path difference values made from multiple roundtrips in the rings and the OPD in the main loop amounting to zero. It is known that the sensitivity of the swept source interferometry is at maximum for zero path difference. This explains the profiles, approximately triangles, located around OPD values where the global path differences are zero.

#135647 - $15.00 USD Received 24 Sep 2010; revised 4 Nov 2010; accepted 12 Nov 2010; published 19 Nov 2010

In Fig. 3a, a decay to half of the value is obtained by moving either side of the maxima by ~7 to 8 mm in all three orders, n = 0, 1 and 2.

At 10% to the right of the maxima, the amplitude of the A-scan curves extend up to 16 to 19 mm for all orders. Some small asymmetries in the curves are noticed, but these can be due to measurement errors. For each order measured, the OPD was varied by acting on the distance between MO3 and MO4. Because the distance between MO3 and MO4 is varied for quite a large distance, of up to 4 cm, distance between the fiber ends behind MO3 and MO4 required readjustment in order to maintain constant reference power. Also, in terms of the width of these curves, we would also expect a slight increase in the coherence length of the interfering waves for higher secondary orders due to the limited bandwidth of the SOAs, comparable to the tuning bandwidth of the swept source. Such a slight increase can be seen by looking at the fall-off at 10% on each curve.

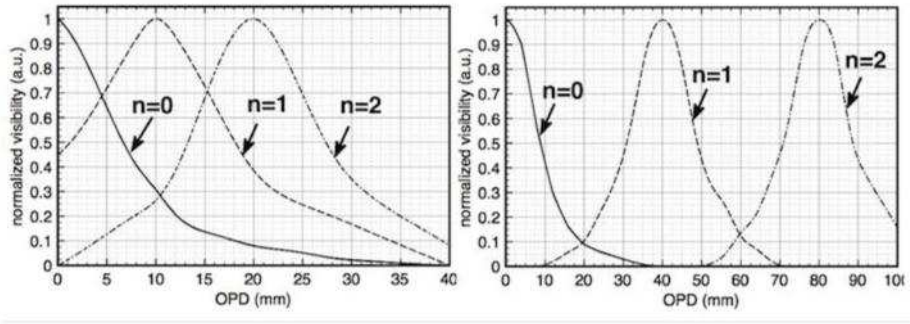

Fig. 3. Normalized visibility versus OPD, for (a): OPD_R = 10 mm and (b): OPD_R = 40 mm.

To separate the axial intervals around each RF carrier, the data in Fig. 3a was repeated for a larger separation of multiple peaks, by extending the OPD_R to - 40 mm, .

Now maxima in OPD are obtained for n = 1 at OPD = 40 mm and for n = 2 at 80 mm. As for Fig. 3b the carrier Δf was set at 500 kHz, when reaching maxima, the frequencies are for n = 1, F_1 = 500 kHz and for n = 2, F_2 = 1 MHz.

Maintaining the same adjustments as in Fig. 3b, by applying signal on the transversal scanner to scan laterally over a mirror, B-scan images were obtained, as shown in Fig. 4. At the top, in 4a, the mirror is at an axial position which falls within the range of sensitivity of the main loop channel. By modifying the length of the reference arm, to investigate deeper objects, two lines are seen in the image at 4b. When OPD matches the opposite value of OPD_R, maximum sensitivity is achieved and the B-scan shows a bright line in 4c for 40 mm. Modifying the length of the reference arm further, two lines can be again observed in 4d, corresponding to the first and the second channel.

For larger values of the OPD, image 4e is obtained, in which case the position of the mirror fits exactly on the position where the second carrier was obtained for OPD = 0 in the 2nd channel, at 80 mm. For this position, a bright line is obtained, in fact the brightest for any other positions within the 2nd channel. In this way, more than 9 cm OPD is covered using the fundamental and two re-circulating loops, i.e. a depth of at least 4.5 cm can be explored (measured in air).

The maximum signal amplitude in each channel (a channel corresponding to each carrier) is given by the decays from one re-circulation to the next, as shown in our previous report on a related configuration [18]. The attenuations from one maximum to the next in Fig. 2, 3 and 4 are ~8 dB. The curves have been drawn normalized in Fig. 3 and 4 to their own maxima for each range. Apart from this decay, the shape of sensitivity versus OPD is similar in all channels and determined by the line-width of the swept source.

The separation of multiple curves in Fig. 2 and 3 in frequency can be adjusted by altering the carrier frequency Δf.

#135647 - $15.00 USD Received 24 Sep 2010; revised 4 Nov 2010; accepted 12 Nov 2010; published 19 Nov 2010

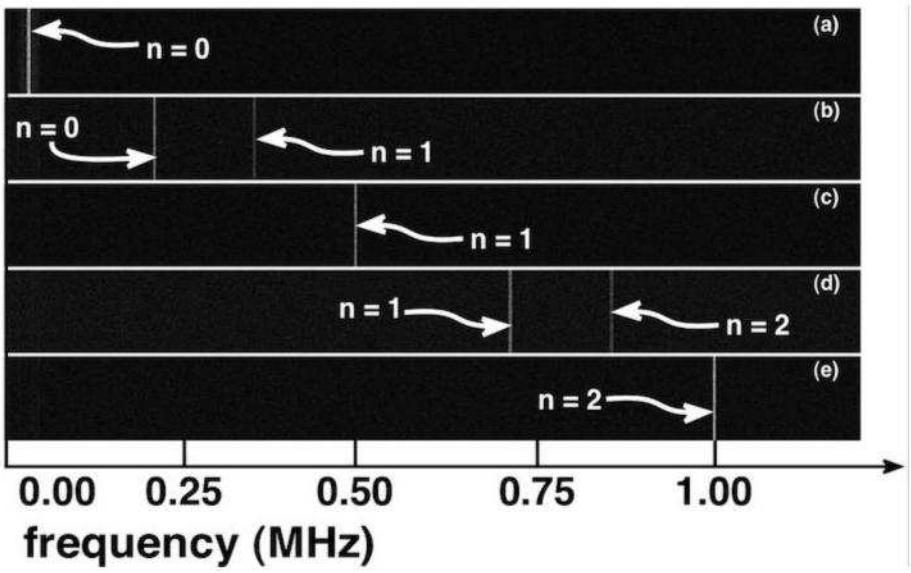

Fig. 4. Long B-scan images obtained for the adjustments in Fig. 3b and Δf = 500 kHz. The five sub-plots have been generated for different OPD values as determined by the axial positions of a flat mirror, corresponding to: (a) OPD = 4 mm (only the first order is present in the image, (b) OPD = 24 mm (both orders, 0 and 1 are present in the image), (c) OPD = 40 mm (only order 1 is in the image), (d) OPD = 64 mm (the first and the second orders are present in the image), (e) OPD = 80 mm (only order 2 is in the image). The horizontal axes at the top show the frequencies corresponding to the three channels, n = 0, 1, 2, centered around their respective carrier frequency values, 0, 500 kHz and 1 MHz, respectively. Each image is formed from 200 A-scans.

Figure 3 and 4 suggest two regimes of operation possible. As obtained with the adjustments used to generate the B-scans in Fig. 4, a 1st regime of operation is that were separate and distinct axial range intervals are obtained. Maximum sensitivity is obtained in each axial interval for OPD = - n·OPD_R, with symmetric decay either side of these values. The maxima from one range to the next decay according to the values of attenuation displayed by the peaks in Fig. 2. By increasing the carrier frequency Δf, the axial intervals in Fig. 3 and 4 can be separated more. A long B-scan image can be generated, however with disjoint intervals of high sensitivity connected by intervals of low sensitivity where similar features from the object are repeated in each channel.

A 2nd regime of operation is that were the two vertical lines in Fig. 4b are superposed.

By changing the OPD, the re-circulation orders shift in frequency by the same amount determined by the conversion factor C. Therefore, once we superposed the orders n = 0 and n = 1 in Fig. 4b for a particular set OPD_R value, they will move within the B-scan together. This requires that:

$$C \cdot OPD = n \cdot \Delta f + C \cdot (OPD + n \cdot OPD_R), \tag{5}$$

which becomes:

$$\Delta f = -C \cdot OPD_R. \tag{6}$$

Such a condition, once accomplished, leads not only to correct images but to an increase in the sensitivity along the depth coordinate, because the larger the OPD in the range up to $|OPD_R|$, the smaller the amplitude in order 0, but larger the amplitude in order 1.

Similarly, for OPD values larger than $|OPD_R|$, the amplitude in order n = 1 decays, but the amplitude in the order n = 2 increases. In fact, condition (6) does not depend on n, this means that for any OPD value, the frequencies generated for all orders coincide.

#135647 - $15.00 USD Received 24 Sep 2010; revised 4 Nov 2010; accepted 12 Nov 2010; published 19 Nov 2010

In this way, taking advantage of the re-circulation loops one can increase the overall axial imaging range in a B-scan image over the value exhibited in the main loop.

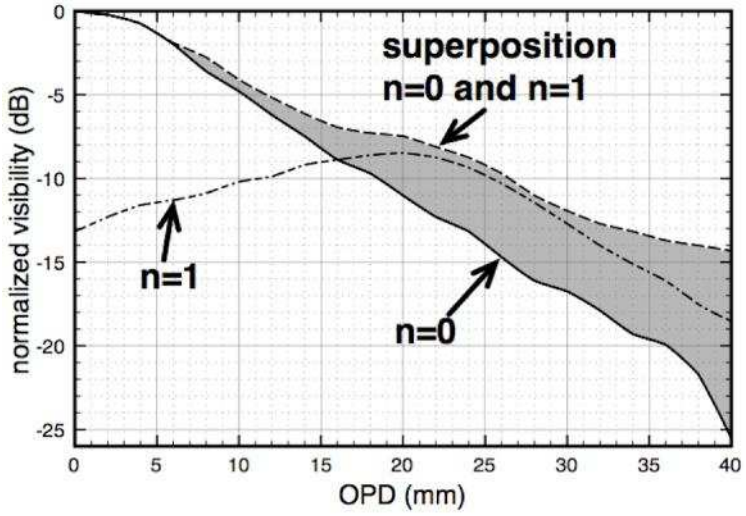

Fig. 5. Visibility profiles vs. OPD, for order 0 and order 1 and for a situation where the two orders have been superposed by choosing the frequency carrier $\Delta f = 180$ kHz and $OPD_R = -20$ mm, to satisfy Eq. (6).

Figure 5 depicts the visibility profiles vs. OPD for the fundamental mode, first re-circulation channel and for the combined fundamental/first channel signal. Initially, the carrier frequency was set at $\Delta f = 250$ kHz. The lengths of the rings were set so that $OPD_R = -20$ mm. In order to superpose the two signals originating from the fundamental channel and from the first re-circulation channel, the frequency of the carrier was altered to 180 kHz to satisfy the condition (6).

Due to the limited instantaneous line-width of the laser output, the maximum axial range of the fundamental channel is limited to 11 mm for a 6 dB attenuation. For an OPD = 20 mm, the visibility in the fundamental channel drops by ~11 dB compared to its value for OPD = 0. On the other hand, the visibility in the combined channel for the same value of the OPD drops by ~7.5 dB only, hence an improvement of ~3.5 dB. For an OPD = 40 mm, the improvement is 10 dB. Further improvement of the overall decay with the OPD could be achieved if attenuation from one channel to the next, as shown in Fig. 2 is diminished. Research is ongoing to understand the factors determining such attenuation with the number of re-circulations. If less attenuation would be achievable for higher orders, then a more extended axial range would be obtained.

Although we still cannot explain exactly why 6-8 dB attenuation is incurred from a round trip to the next, if this could not be improved, then another possibility, when working on only a few orders, such as n = 0, 1 and 2 would be to balance the contributions of at least these orders to the final signal. We noticed that polarization controllers can be used with some effect to modify the distribution of power between the main component and the components from the secondary loops. Another possible avenue would be to change the coupling ratio of DC1 and DC2 and use higher gain and higher saturation power SOAs. In this first implementation, the coupling ratio was 50/50. By changing this ratio, the balance of powers from the swept source and from the SOAs can be modified. In this way, the contribution of waves from the secondary trips can be made to count more in comparison with the power from the swept source. This could increase the contribution of at least the first lower recirculating orders in comparison to the main loop.

However, as it is, the configuration in Fig. 1 allows a larger strength signal by combining the orders n = 1 and n = 2, than by using the signal determined by the main loop only.

#135647 - $15.00 USD Received 24 Sep 2010; revised 4 Nov 2010; accepted 12 Nov 2010; published 19 Nov 2010

To prove the capability of the system to produce enhanced axial range images, we imaged a rectangular slab of resin with a high concentration of scattering titanium dioxide. Figure 6 shows such B-scan images. Images having subscript 1 correspond to the superposed signal, while images with subscript 2 correspond to the fundamental channel only. In order to create a meaningful image, we needed to increase the number of A-scans in the B-scan. Because the tuning speed of the swept source used here is limited, we reduced the tuning bandwidth to 25 nm. This has allowed us to increase the number of A-scans in the B-scan to 400 Hz in 1 s.

To enhance the signal from deeper levels in the sample, we adjusted the reference path shorter than the object path in the main loop. In this way, the deeper layers, which return less back scattered signal, are closer to OPD = 0 and are favored by enhanced sensitivity, as the sensitivity decays from a maximum at OPD = 0 in the main loop and from the OPD values corresponding to $-n \cdot OPD_R$.

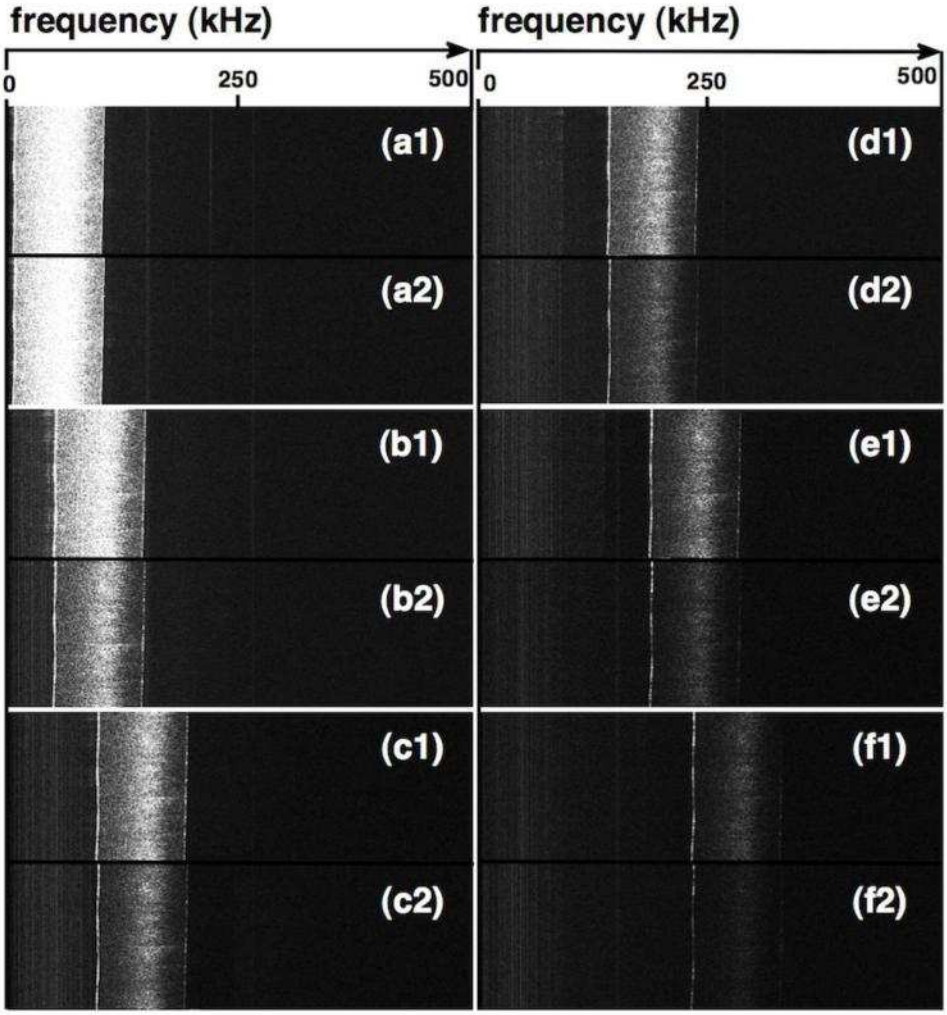

Fig. 6. B-scan images of the TiO_2 based sample of thickness 4 mm. The horizontal size of the images is 27.62 mm depth, measured in air. The horizontal axis extends on the right up to 500 kHz. (a1) and (a2) correspond to OPD = 1 mm (the back surface of the sample was placed at OPD = 1 mm), then the length of the reference arm was altered by: 5 mm in (b1,2), 10 mm in (c1,2), 15 mm in (d1,2), 20 mm in (e1,2) and 25 mm in (f1,2). The images with subscript 1 correspond to the combined channel while those with subscript 2, to the fundamental channel.

#135647 - $15.00 USD Received 24 Sep 2010; revised 4 Nov 2010; accepted 12 Nov 2010; published 19 Nov 2010

Figures 6(a1) and 6(a2) shows the sample, with the backside towards OPD = 0 (to the left and its top to the right). The enhanced band within the sample shows the profile of the confocal gate, determined by the interface optics and the fiber aperture. As we progress in depth in the sample (towards right), the image looses brightness in Fig. 6(b1) and 6(b2). However it is obvious that at the maximum depth in the sample, Fig. 6(b1) is slightly brighter than Fig. 6(b2). As the top part of the sample corresponds in 6(d1, d2) to an OPD ≈26.2 mm, the improvement in terms of visibility, as predicted by Fig. 5 is 5 dB. The enhancement is due to the first re-circulation channel, which adds up to the intensity, improvement that becomes more visible in the next images. In Figs. 6(d2) and 6(e2), the sample in the B-scan is barely visible while it cannot be distinguished at all in Fig. 6(f2).

5. Conclusion

We presented a novel swept source interferometry configuration whose key element is the use of re-circulation loops in both sample and reference arms. The configuration acts by replicating and extending the coherence length of the swept source driving it. In this way, such a configuration presents the potential of a much longer axial imaging depth than the limit imposed by the coherence length of the swept source. The configuration can also be set to deliver distinct images for different axial intervals. We demonstrate the enhancement capability in terms of the axial range of the configuration by producing a long B-scan with signals contributed from the main loop and from the first two re-circulations, i.e. the B-scan so produced was approximately three times deeper than the one in the main loop. Further research is required to enhance the amplitude of higher number of roundtrips. If that would be achievable, then lower cost swept sources, with relatively wide line-width, determining small axial length values such as for example 0.5 mm only, could be used in conjunction with such a configuration to image more than 1.5 mm, to cover the most spread range of OCT applications, with sufficient sensitivity. For the OCT, we estimate that no more than 4 orders would be required with lower attenuation in between than that obtained in this proof of concept configuration. For sources with narrow line-width, like the one used here, extremely long axial range could become possible, extending over a couple of cm, however faced with the problem of a limited focus depth range.

Acknowledgments

Adrian Bradu acknowledges Engineering and Physical Sciences Research Council, United Kingdom, grant EP/H004963/1. Liviu Neagu acknowledges the Marie Curie Training site MEST-CT-2005-02035. The authors also acknowledge the support of Superlum Moscow, Cork, Ireland, which has loaned the swept source for this study, and Mohammad Reza Avanaki for preparing the resin sample.

#135647 - $15.00 USD Received 24 Sep 2010; revised 4 Nov 2010; accepted 12 Nov 2010; published 19 Nov 2010